The 5th European sCO2 Conference for Energy Systems
March 14-16, 2023, Prague, Czech Republic

2023-sCO2.eu-146

DESIGN OF COMPACT RADIAL TURBOEXPANDERS FOR SCO2 POWER SYSTEMS

Alessandro Romei
Giacomo Persico*
Politecnico di Milano
Milan, Italy

Davide Biliotti
Alberto Milani
Baker-Hughes Nuovo Pignone
Florence, Italy

Fabrizio Lottini
Michele Marconcini
Università degli studi di Firenze
Florence, Italy

ABSTRACT

The development of novel conversion technologies for recovering waste heat is one of the technical goals of the European Commission, considering the large amount of thermal energy discharged by industrial processes in Europe. The recently launched EU-H2020 project CO2OLHEAT aims at contributing to industrial waste heat recovery by developing a novel sCO2 power system of 2 MW power capacity. Considering the wide range of conditions featuring waste heat recovery applications (in terms of both flue gas temperature and flow rate), as well as the flexibility of operation required by such installations, a simple recuperative cycle was selected for the CO2OLHEAT plant. The system, however, features a relatively non-conventional multi-shaft configuration, composed of a radial-inflow turboexpander, which drives the near-critical compressor, and by an axial-flow turbine to generate the 2 MW output power.

The present study focuses on the design of the radial turbines of the CO2OLHEAT turbo-expander. Due to the low volumetric flow rate, the turbine features small size and, therefore, significant aerodynamic challenges have to be considered in the design process. A preliminary design of the machine was performed by applying a mean-line approach, then a conceptual design of the bladings and of the meridional channels was performed by resorting to industrial in-house database and criteria. Once the turbine design was finalized, the aerodynamics and performance of the machine were evaluated by applying two different computational fluid dynamic simulation tools, which exhibit remarkable agreement.

One CFD tool was then used to investigate and quantify the impact of wheel tip clearance and surface roughness, as well as to quantify the deviation with respect to mean-line predictions. Relevant quantitative data are extracted as well as aerodynamic indications are inferred, with the aim of establishing a reference for the future design of compact sCO2 radial turbines.

INTRODUCTION

The industrial sector in Europe releases in the environment a large amount of waste heat, as a result of the thermal processes involved in the production of cement, glass, steel, etc. The flue gases discharged by such processes are released in a wide temperature range and could be efficiently and effectively converted into useful mechanical or electrical energy. On the quantitative ground, considering recent statistics on waste heat not exploited [1], and assuming an average conversion efficiency of 25% with an operating factor of 0.8, the conversion of 5% of the European waste heat would lead to more than 500 GWh of primary energy savings per year and, assuming 0.46 tCO2/MWh, it would avoid more than 100.000 tons of CO2 per year. It would also provide important economical relapses, further enhanced by the recent severe increase of fossil-fuel prices.

Mature technologies are presently available for waste heat recovery and conversion, in particular Organic Rankine Cycles and conventional Steam Rankine Cycles; however, the former guarantee effective performance especially for flue gas temperature below 300°C, while the latter are best optimized for flue gas temperature above 500°C. As a result, in the temperature range 300-500°C, which represents a large share of the overall available waste heat, alternative technologies might provide better effectiveness, both technically and economically. Among them, closed Joule-Brayton thermodynamic cycles working with carbon dioxide in supercritical conditions (sCO2) are particularly attractive due to the expected cycle efficiency and the overall system compactness, which might foster fast response to transients and reduced footprint, crucial features for effective waste-heat recovery systems [2].

Even though advanced calculations were performed at both system ([3], [4]) and component ([5], [6], [7], [8]) level, and the first experimental verification of components have given promising outcomes (especially for the compressor, see [9], [10]), a proper demonstration of the overall system operation in the real environment is still needed. To this end, the EU-H2020 project CO2OLHEAT (Supercritical CO2 power cycles demonstration in Operational environment Locally valorising

* corresponding author: giacomo.persico@polimi.it

DOI: 10.17185/duepublico/77327

This work may be used under a Creative Commons Attribution 4.0 License.

industrial Waste Heat) was launched in 2021, with the aim of developing a novel sCO2 power system demonstration plant of 2-MW capacity, to be installed and operated in a real industrial environment, recovering waste heat from flue gases released at about 400 °C. By considering the flue gas conditions, as well as the required flexibility of operation, a simple recuperative sCO_2 cycle has been selected for the CO2OLHEAT system, with the sCO_2 compressor powered by a radial turboexpander and a subsequent axial turbine for electrical power generation.

The present study focuses on the design of the sCO_2 radial turbines used to drive the CO2OLHEAT compressors, which combined constitute the turbo-expander unit of the system. The design of sCO_2 turbines has to face different challenges with respect to sCO_2 compressors. The fluid, even though highly pressurized, is usually in a thermodynamic state sufficiently far from the critical point, so that the ideal-gas model becomes accurate to represent the fluid behavior and no phase change process can occur. The limited overall pressure ratio (of the order of 3—4 for sCO_2 systems, and 2.55 in the present case) combined with the multi-stage configuration greatly limit the Mach number, avoiding transonic effects. This, however, does not make the design of these machines straightforward: the high density of the fluid has relevant implications on aerodynamics (low aspect ratio bladings, high leakage flow rates in the seals), structural integrity (high aerodynamic forcing), and rotordynamics (high vibration and stress in the bearings) [11]; the combination of high temperature and high density makes critical the selection of the material for blades and casing [12].

The relative weight of these features changes depending on the turbine architecture, so the preliminary selection of the machine configuration is crucial to construct a turbine design tailored to sCO_2 applications. As discussed in the next section, the characteristics of the thermal source, preliminary considerations on the primary heat exchanger, and the thermodynamic optimization of the cycle led to select the turbine intake state at 216.9 bar and 360°C. Given the small power capacity, the low volumetric flow rate, and the limitations in angular speed, statistical and similarity considerations recommend selecting a radial-inflow architecture for these turbines. The two resulting turbines were, therefore, designed by leveraging the Baker Hughes experience on expanders, with a special focus on structural and rotordynamic aspects; however, the compactness of the machine suggested investigating the impacts of the tip clearance and wall roughness.

The paper reviews the turbine design process and it is structured as follows: at first the CO2OLHEAT system is presented and the turbine configuration is described; then, the turbine aerodynamics and performance are analysed by discussing the results of three computational models, namely one mean-line and two CFD simulation tools, to provide a multi-fidelity perspective of the turbine operation. Then, size effects related to tip clearance and wall roughness are analysed and quantitatively discussed.

CO2OLHEAT POWER UNIT

The CO2OLHEAT power unit was conceived to recover waste heat from an existing cement plant, whose flue gases in nominal conditions are available at temperature of 400°C and with a flow rate of 230,000 Nm^3/h. The core of the system is a simple recuperated cycle without either recompression or recuperator bypass, due to the relatively low maximum temperature of the heat source and the high minimum stack temperature to avoid acid condenses (150°C). As reported in Figure 1, in the overall system the power unit is complemented by a waste-heat recovery unit and by a water-based heat-rejection unit.

The thermodynamic optimization of the sCO_2 cycle led to setting the compressor-intake thermodynamic conditions at 32°C and 85 bar respectively, to properly exploit the high density of CO_2 in the proximity of the critical point. The compressor-outlet pressure is set to 216.9 bar, resulting from a trade-off between cycle performance, material selection, and cost. The resulting cycle pressure ratio is equal to 2.55, which is obtained by two centrifugal compressors in series; they are mechanically driven by two centripetal turbines in series, thus creating a compact turbo-expander unit. The maximum temperature of the cycle is set at 360°C, namely 40°C lower than the flue gas nominal temperature in order to limit the surface area of the primary heat exchanger. The expansion is completed in an axial turbine, which is responsible for the power output of the system.

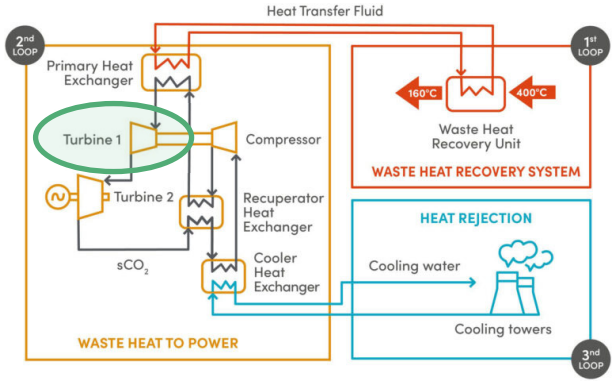

Figure 1: CO2OLHEAT concept – the focus is on turbine 1 (turboexpander).

The resulting net power output exceeds 2 MW, with a cycle efficiency of 23.2% referred to the inlet thermal power. Full details on the CO2OLEAT power system design and off-design operation can be found in [13].

MACHINE ARCHITECTURE

The optimization of selected thermodynamic cycle requires the compressor to operate between 85 and 216.9 bar with inlet conditions very close to CO_2 critical point (32°C, 670 kg/m^3). The inlet conditions of the expander that will drive the compressor are consequently at 210.0 bar, 360°C. Actual process conditions and demo site available power lead to compact machine size with compressor impeller diameter lower than 150

DOI: 10.17185/duepublico/77327

mm and a rotating speed close to 20,000 RPM, and an expander impeller diameter in the range of 160-170 mm and a rotating speed close to 12,500 RPM. To minimize the impact of internal leakages and to manage residual axial thrust, an integrally geared configuration has been selected, which includes two shaft, one dedicated to compression section and one to expansion phase.

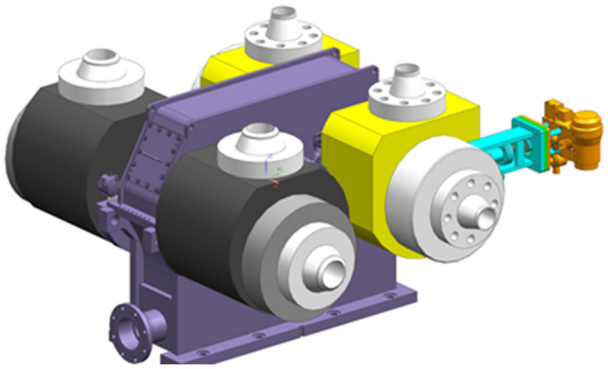

Figure 2: Machine schematic
© 2022 Baker Hughes Company - All rights reserved

The overall pressure ratio, for both compressor and expander, has been split into two stages in back-to-back arrangement. First compression phase is equipped with movable axial inlet guide vane (IGV) to guarantee a fine tuning of the suction operating condition, and to improve compressor flexibility in off-design conditions. No movable nozzles are provided at the inlet of the two expander stages.
The integrally geared arrangement has a starter motor connected to the low-speed shaft. To maintain the operating speed of the machine constant during operation, the electric motor will take care of around 20% of the compressor absorbed power, acting as a helper motor. The remaining power, to sustain the compressor, will be provided by the expander wheel.

TURBOEXPANDER DESIGN

The design of the turbo-expander is realized by Baker Hughes. The first step is turbine selection. From the boundary conditions of the machine, the size and rotational speed of the turbo-expander are calculated. This phase relies on correlations and graphs proprietary of Baker Hughes. In particular, the expected efficiency η_{TS} of the machine is a function of the specific speed N_s, defined as:

$$N_s = \frac{N\sqrt{Q_{t5}}}{\Delta h^{3/4}} \tag{1}$$

The relationship between the efficiency η_{TS} and the specific speed N_s is shown in Figure 3. There is an optimum value of the specific speed, which guarantees the best performance. In particular, the specific speed value is selected where the stage performance curve is flat. Once a suitable value of N_s is chosen, the rotational speed N is known.

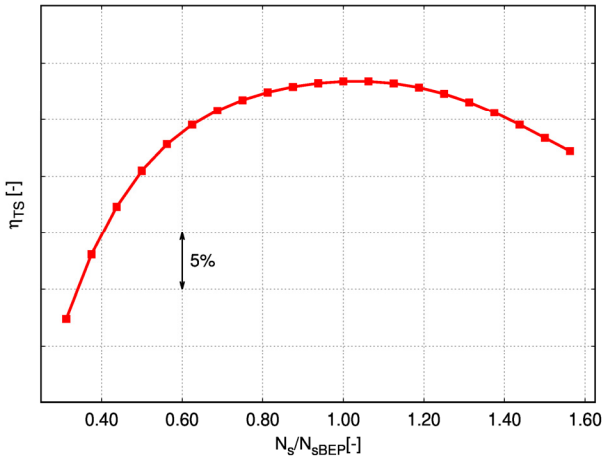

Figure 3: Efficiency η_{TS} as a function of the specific N_s
© 2022 Baker Hughes Company - All rights reserved

The specific speed is experimentally connected to the ratio u/c, where c is the spouting velocity, defined as:

$$c = \sqrt{2 \cdot (h_{t0} - h_{5,is})} \tag{2}$$

This quantity corresponds to the flow velocity if the entire enthalpy drop was realized by the nozzle vanes.

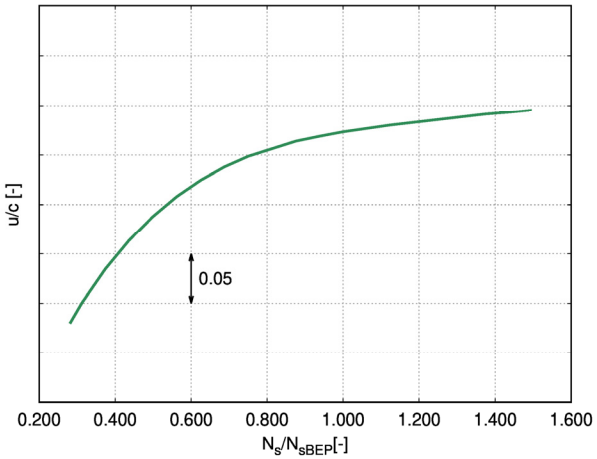

Figure 4: u/c ratio as a function of the specific speed N_s
© 2022 Baker Hughes Company - All rights reserved

With the specific speed value it is possible to enter the graph in Figure 4 to obtain a value of the ratio u/c. Since the isentropic enthalpy drop of the stage and the rotational speed are known, a value for the wheel outer diameter D_3 can be calculated.
The boundary conditions together with the information derived from the selection phase (N, D_3, η_{TS}) constitute the input required by the Baker Hughes preliminary design tool. This tool

DOI: 10.17185/duepublico/77327

uses a 1D analysis of the turbo-expander stage to generate the geometry for the nozzle vanes and the wheel. The stage geometry is designed to ensure a negative incidence angle on wheel blades, an almost axial flow at the rotor outlet, and an optimal value for the ratio between the wheel outlet hub diameter and the rotor outer diameter D_{5h}/D_3. Further details on the preliminary design tool are reported in [14]. A simple convergent profile is designed for the nozzles because of low expansion ratios. Figure 5 shows a view of the geometry generated for the present activity.

Figure 5: Three-dimensional view of the stage geometry
© 2022 Baker Hughes Company - All rights reserved

NUMERICAL METHODS

In this section, the numerical methods that are used to carry out the design and performance analysis of the radial turboexpander are discussed.

Mean-Line Model

A mean-line model is used to estimate the performance of the turbine at a preliminary stage. The tool is written in *python* language, making use of its library and modules for root-finding algorithms and minimization. The thermodynamic and flow conditions at each section along the machine are computed at the mean-line in the stage meridional plane and are representative of mass-weighted averaged conditions over the whole section.

The tool focuses on the modelling of nozzles, the nozzle-rotor interspace, and the rotor. Figure 6 shows a scheme of the radial turbine flow path illustrating the main sections, the terminology, and the symbols used in the following.

The thermodynamic and flow conditions at the main sections in the stage are calculated by solving simultaneously the mass continuity, the energy balance, and the loss equations. The fluid properties are computed using the real gas modeling of the REFPROP library [15]. The following working input variables are required by the mean-line model: inlet total pressure p_{t0}, inlet total temperature T_{t0}, outlet static pressure p_{s5}, rotational speed N, tip clearance if present, number of nozzles Z_N and wheel blades Z_W. Moreover, the code takes input also from the geometry of the stage, described with the nozzles profiles, the wheel blade profiles at the hub and tip sections, and the stage flow path. For each section along the stage, a system of equations is resolved. The first set of equations is applied to the nozzle throat section, and consists of the following equations:

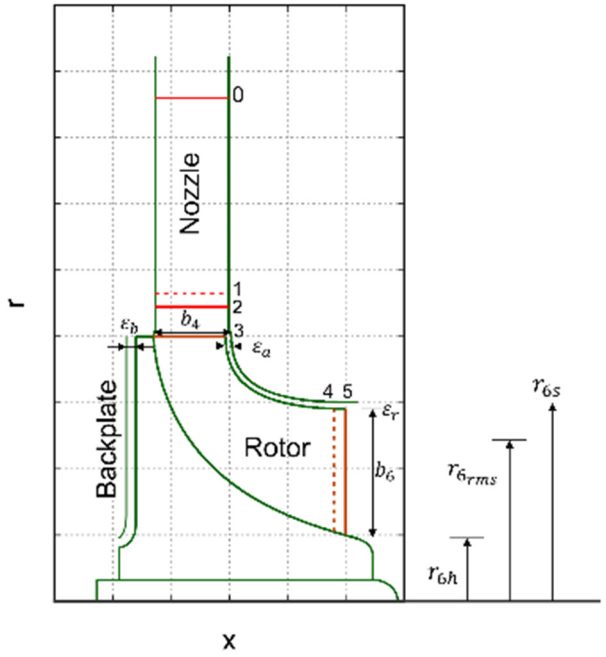

Figure 6: Schematic flow path of a radial in-flow
© 2022 Baker Hughes Company - All rights reserved

$$c_1 = \frac{\dot{m}}{\rho_1 \cdot A_1 \cdot (1 - BF_1)} \tag{3}$$

$$h_1(\rho_1, T_1) = h_{t0} - \frac{1}{2} c_1^2 \tag{4}$$

$$\sum_{1}^{n_L} \Delta h_{loss_N} + h_{1_{is}}(p_1, s_0) - h_1(\rho_1, T_1) = 0 \tag{5}$$

The term $\Delta h_{loss,n}$ represents the specific loss contribution in the blade row, which is calculated through an empirical correlation. All the loss correlations used in the model are reported in Table 1. The flow angle in section 1 for the nozzle is predicted using the cosine rule:

$$\alpha_1 = \cos^{-1}(o_1/s_1) \tag{6}$$

where o_1 is the nozzle throat opening and s_1 is the vane circumferential spacing.

The nozzle vanes resolution is based on the continuity (3), the equation of energy (4), and the loss equation (5). This system of equations can be graphically described by Figure 7.

DOI: 10.17185/duepublico/77327

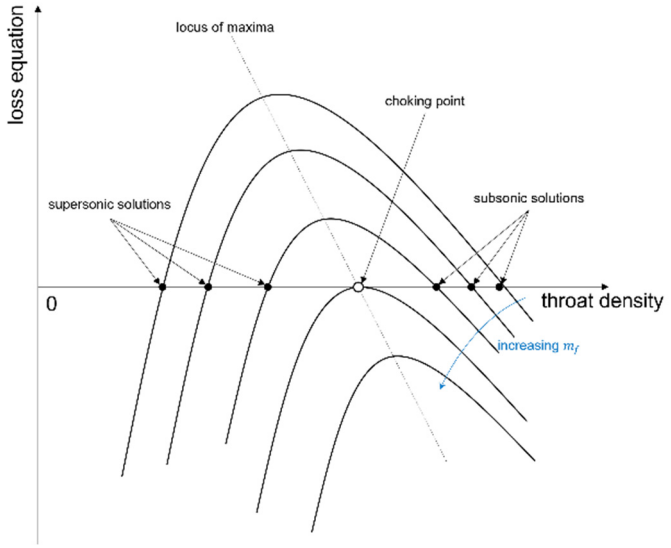

Figure 7: Solutions for a blade row section in the mean-line model.

Each curve in the graph of Figure 7 refers to a given mass flow rate. As the mass flow rate increases, the curve shifts downward. For a very high mass flow rate, the curve lays entirely below the x-axis, meaning that no solutions can be found. The choke condition corresponds to the curve being tangent to the 0 of the loss equation. For higher values of the mass flow rate, two solutions can be found. The solutions that are on the left with respect to the curve maximum refer to the supersonic solutions, which are not physical since the model only considers convergent profiles. The solutions on the right side of the curve maximum are the subsonic solutions, so they represent the actual solutions of the system.

If the nozzle vanes are choked, a post-expansion takes place after the nozzle throat. In this case, the energy and mass balances and the post-expansion loss equation are solved, respectively as follows:

$$c_2 = \sqrt{2 \cdot (h_{t0} - h_2(p_2, \rho_2)}$$ (7)

$$\alpha_2 = \cos^{-1}\left(\frac{m}{\rho_2 \cdot c_2 \cdot A_1 \cdot (1 - BF_1)}\right)$$ (8)

$$\Delta h_{pe_N} + h_{2_{is}}(p_2, s_1) - h_2(\rho_2, p_2) = 0$$ (9)

After the nozzle, the flow continues its expansion in the vaneless space before entering the wheel. The expansion in this interspace can be modelled using the following set of equations:

$$c_3 = \frac{\dot{m}}{\rho_3 \cdot \cos\alpha_3 \cdot A_3 \cdot (1 - BF_3)}$$ (10)

$$\frac{c_2 \cdot \sin\alpha_2}{c_3 \cdot \sin\alpha_3} = \frac{r_3}{r_2} + \frac{2\pi C_f \cdot \rho_3 c_3 \sin\alpha_3 \,(r_2^2 - r_2 r_3)}{\dot{m}}$$ (11)

$$h_3(\rho_3, T_3) = h_{t0} - \frac{1}{2}c_3^2$$ (12)

$$\Delta h_{loss_{VS}} + h_{3_{is}}(p_3, s_2) - h_3(\rho_3, T_3) = 0$$ (13)

Equation (11) represents the Stanitz correlation [16] for the correction of the flow angle in the conservation of the momentum.

The set of equations for the rotor resolution is the same as the nozzle vanes, but referred to the relative frame:

$$w_4 = \frac{\dot{m}}{\rho_4 \cdot A_4 \cdot (1 - BF_4)}$$ (14)

$$h_4(\rho_4, T_4) = I_3 - \frac{1}{2}w_4^2 + \frac{1}{2}u_4^2$$ (15)

$$\sum_1^{n_L} \Delta h_{loss_W} + h_{4_{is}}(p_4, s_3) - h_4(\rho_4, T_4) = 0$$ (16)

where $I = h + \frac{1}{2}w^2 - \frac{1}{2}u^2$ is the rothalpy. The term $\Delta h_{loss,r}$ represents the specific loss contribution in the rotor, which is calculated using empirical correlations for each loss source described in Table 1. The exit relative flow angle in section 4 is evaluated using the cosine rule:

$$\beta_4 = \cos^{-1}(o_4/s_4)$$ (17)

where o_4 is the wheel throat spacing and s_4 is the rotor pitch at the throat section. In case of the rotor choking point is reached, the mass flow rate is kept constant, and the nozzle operation is fixed since any further expansion downstream of the wheel cannot affect the conditions upstream of the rotor throat.
In this case of a choked rotor, any further expansion is allowed by means of a post-expansion process after the wheel throat, which is resolved using the following set of equations:

$$w_5 = \sqrt{2 \cdot \left(I_4 - h_5(p_5, \rho_5)\right) + u_5^2}$$ (18)

$$\beta_5 = \cos^{-1}\left(\frac{m}{\rho_5 \cdot w_5 \cdot A_4 \cdot (1 - BF_4)}\right)$$ (19)

$$\Delta h_{pe_W} + h_{5_{is}}(p_5, s_4) - h_5(\rho_5, p_5) = 0$$ (20)

DOI: 10.17185/duepublico/77327

Loss source	Loss model	Reference
Nozzle passage	$\Delta h_{pl,\,noz} = K_{p1}\frac{0.05}{Re_1^{0.2}}\left[\frac{3\tan\alpha_1}{\sigma_1/c_n}+\frac{\sigma_1\cos\alpha_1}{b_1}\right]\frac{1}{2}c_1^2$	Rodgers [17]
Nozzle trailing edge	$\Delta h_{te,N} = \left(\frac{Z_n t_2}{2\pi r_2\cos\alpha_2}\right)^2\frac{1}{2}c_2^2\cdot Y_2$	Glassman [18]
Nozzle post-expansion	$\Delta h_{pe,N} = \left(\frac{M_2-M_1}{M_2}\right)^2\frac{1}{2}c_2^2\cdot\frac{1}{Y_2}$	Aungier [19]
Interspace	$\Delta h_{vs} = K_{vs}C_f\left(\frac{L_{vs}}{D_{vs}}\right)\frac{1}{2}\left(\frac{c_2+c_3}{2}\right)^2$	Kastner and Bhinder [20]
Rotor incidence	$\Delta h_{inc,W} = K_{inc}\left(\sin\lvert\beta_3-\beta_{3,opt}\rvert\right)^2\frac{1}{2}w_3^2$	Baines [21]
Rotor passage	$\Delta h_{pl,W} = K_p\left\{K_{p2}\left(\frac{L_H}{D_H}\right)+0.68\,K_{p3}\left[1-\left(\frac{r_{4_{rms}}}{r_3}\right)^2\right]\left(\frac{\cos\beta_4}{b_4/ch_W}\right)\right\}\frac{1}{2}(w_3^2+w_4^2)$	Baines [21]
Rotor clearance	$\Delta h_{cl} = \frac{u_3 Z_W}{8\pi}\left(K_a\varepsilon_a C_a + K_r\varepsilon_r C_r + K_{ar}\sqrt{\varepsilon_a\varepsilon_r C_a C_r}\right)$	Baines [21]
Rotor trailing edge	$\Delta h_{te,W} = \left(\frac{Z_W t_5}{\pi(r_{5_s}+r_{5_h})\cos\beta_5}\right)^2\frac{1}{2}w_5^2\cdot Y_5$	Glassman [18]
Rotor disk friction	$\Delta h_{df} = 0.25\,K_f\frac{\bar\rho u_3^3 r_3^2}{\dot m}$ where $\bar\rho = \frac{\rho_3+\rho_5}{2}$ $Re_4 = \frac{\rho_3 u r_3}{\mu_3}$	Aungier [19]
Rotor post-expansion	$\Delta h_{pe,W} = \left(\frac{M_{5_{rel}}-M_{4_{rel}}}{M_{5_{rel}}}\right)^2\frac{1}{2}w_5^2\cdot\frac{1}{Y_5}$	Daily and Nece [22]

Table 1: Loss models for a radial in-flow turbine.

The loss models are summarized in Table 1. Details on the values of loss coefficients K_i reported in Table 1 can be found in [23] and [24]. The validation of the mean-line model based on several experimental test cases available in literature is described in [23].

TRAF Code

The TRAF code is a RANS/URANS viscous multi-block flow solver for the 3D Reynolds-averaged Navier-Stokes equations developed at the University of Florence [25]. Real gas behavior can be modelled by providing gas property tables generated offline [26]. Steady-state analyses with a perfect gas model are carried out in the present activity. Uniform total pressure and total temperature distributions of a radial inflow are applied at the domain inlet section. A static pressure value is applied at the hub radius of the domain outlet section and the radial equilibrium is used to obtain the spanwise pressure distribution. The rows coupling is handled by means of a mixing plane. The code has been previously used to calculate subsonic and supersonic turbo-expander stage flows [27] [28] [14].

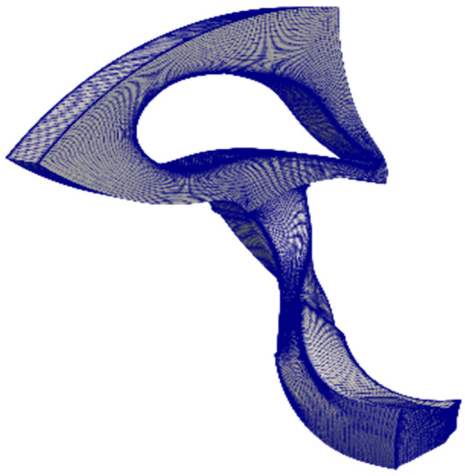

Figure 8: CFD grid for TRAF calculations.
© 2022 Baker Hughes Company - All rights reserved

The convective fluxes are resolved using a 2nd order TVD-MUSCL strategy built on top of the Roe's upwind scheme [29].

DOI: 10.17185/duepublico/77327

The high-Reynolds formulation of the Wilcox k − ω model [30] is used for the turbulence closure.

The CFD grid is composed of about 4.5 M cells. An O-type structured grid of ~3 M is adopted for the nozzle vane, while a ~1.4 M H-type structured grid is used for the rotor passage. The first cell distance from the wall is imposed to ensure a y+ < 1 on solid walls. The fillets on the wheel blades are included in the model. Figure 8 shows the computational grid investigated by the CFD simulations.

CFD – POLIMI

The computational flow model is based on the ANSYS-CFX finite-volume flow solver, using high-order numerical schemes for both inviscid and viscous fluxes. Turbulence effects are introduced by resorting to the $k-\omega$ SST model assuming fully turbulent flows. Whenever walls are modelled as smooth, the turbulence equations are resolved at the wall having wall-adjacent cells in the viscous sublayer, i.e. $y^+ \sim 1$. Otherwise, wall functions are employed to account for roughness effects.

In the thermodynamic conditions of interest, CO_2 behaves as a polytropic ideal gas (compressibility factor ~ 1.0). Therefore, the perfect gas model with $\gamma = c_p/c_v = 1.181$ is employed for the thermodynamic properties. Due to the small temperature drop across the expansion, constant values for the transport properties are assigned. A comparative assessment was carried out using look-up tables built on the basis of real-gas property estimates by REFPROP. Deviations below 0.1% confirmed the suitability of the perfect gas model as a thermodynamic model for subsequent analyses.

Radial inward flow is prescribed at the nozzle inlet together with total pressure and temperature. No-slip and adiabatic boundary conditions were imposed on the solid walls. A static pressure is specified at the midspan outlet radius, imposing a pressure distribution along the span that complies with the radial equilibrium. A mixing-plane interface is placed halfway between the nozzle and the wheel. Across this interface, the velocity from the nozzle outlet is circumferentially averaged and passed as an inlet boundary condition to the wheel inlet together with the averaged static pressure. The circumferential average enables the simulation of a single nozzle and wheel passage by imposing periodic boundary conditions likewise to the computational domain reported in Figure 8.

Both nozzle and wheel mesh are generated with Ansys Turbogrid and are made of hexahedral elements. The computational grid of the wheel includes fillets. Whenever an open wheel is simulated, the clearance gap is discretized with 35 grid points with proper cell clustering near walls to account for the viscous sublayer. A dedicated grid study has shown that a nozzle mesh composed of 2.5 million cells plus a wheel mesh composed of 3.1 million cells provide a grid convergence index for the total-to-total efficiency equal to 0.10%.

TURBINE PERFORMANCE

In this section, the performance of the high-pressure turbine that will be part of the CO2OLHEAT demo plant is discussed. In the early stages of the design phase, an open wheel was taken into consideration because of the medium temperature level combined with the small size. A shrouded design was ultimately selected after a careful assessment of stresses and corresponding deformations. The high-pressure and low-pressure stages feature similar design aspects and performance, therefore only the high-pressure turbine will be discussed.

Figure 9 reports the trend of total-to-static efficiency and the ratio u/c across the flow range. CFD results are obtained by extracting mass-weighted averages of relevant quantities from corresponding sections as illustrated in Figure 6. The only exception is the static pressure, for which the area-weighted average is considered. The two independent CFD studies agree remarkably well in predicting both η_{TS} and u/c. Differences are below 0.2%, fostering our confidence in the numerical results.

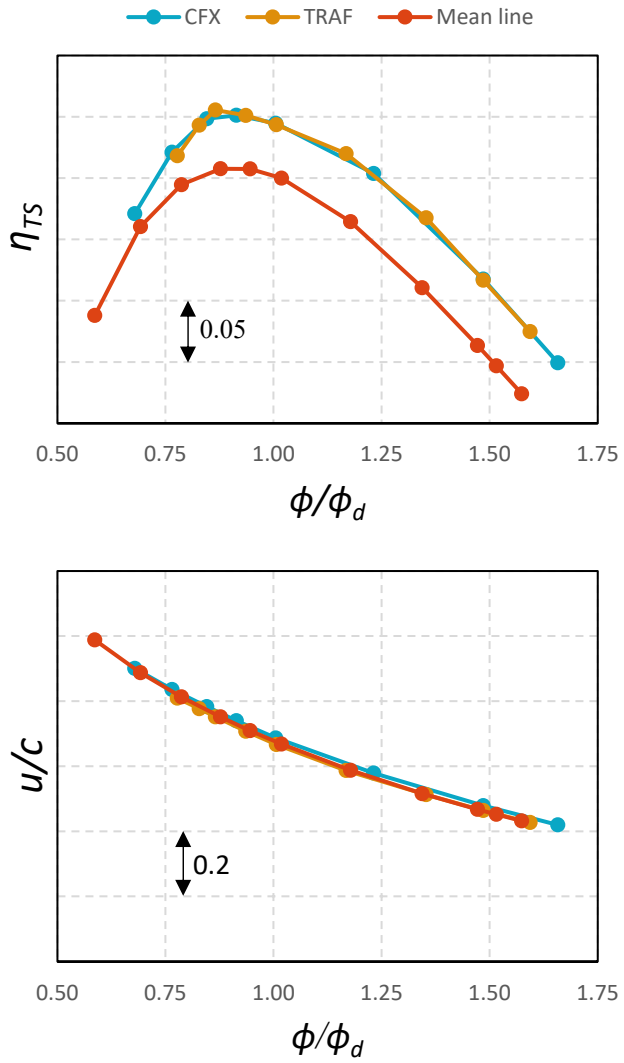

Figure 9: Total-to-static efficiency and u/c ratio across the normalized flow range as predicted by two independent CFD studies (different codes and meshes) and by the mean line.

© 2022 Baker Hughes Company - All rights reserved

DOI: 10.17185/duepublico/77327

Looking at CFD trends, it can be noted that, even when the flow rate increases by 75% with respect to the nominal one, the turbine is not choked. This is due to the relatively small expansion ratio across the turbine, which in turn elaborates a subsonic flow ($M < 0.3$), as highlighted by the Mach number field in Figure 10. Therefore, the efficiency keeps reducing almost linearly after $\phi/\phi_d > 1.25$, with an efficiency drop of 10% for each 25% flow increase. The peak efficiency is at $\phi/\phi_d \sim 0.9$. This choice allows a higher efficiency at part load conditions, for which the efficiency drop is more pronounced than the one at higher flow rates.

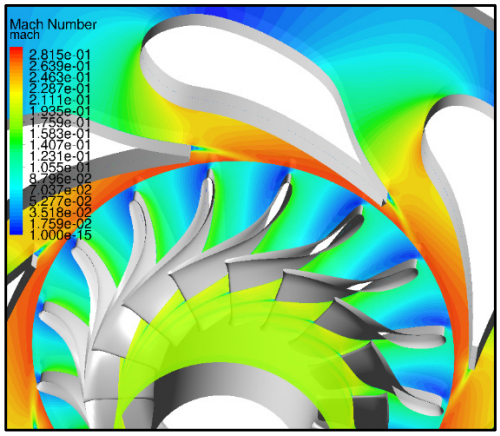

Figure 10: Flow fields in terms of relative Mach number at midspan in nominal conditions.
© 2022 Baker Hughes Company - All rights reserved

Finally, the mean line predicts trends across the flow range that are consistent with the CFD predictions, but it returns comparably smaller efficiencies, which are reduced by 5% percent. Opposed to such efficiency discrepancy, the trend u/c is well reproduced by the mean line model. It is worth noting that u/c is directly correlated with the internal aerodynamics that is simulated via CFD calculations, while the mean-line efficiency includes additional loss sources which occur outside the CFD domain, namely disk and casing friction. Therefore, the good matching between CFD and mean-line in predicting u/c serves as verification of the mean-line tool, which can be then used to have a more realistic representation of the stage efficiency by including external loss mechanisms.

SIZE EFFECTS (CLEARANCE AND ROUGHNESS)

Owing to the small size of sCO_2 turbines, the effect of non-scalable geometrical parameters, such as roughness and, possibly, clearances, are expected to significantly affect the turbine efficiency. In this section, such classes of efficiency penalties are quantified, by considering four cases:

- Open wheel with $\varepsilon_r/D_{wheel} = 0.03$, smooth walls
- Shrouded wheel, smooth walls
- Open wheel with $\varepsilon_r/D_{wheel} = 0.03$, rough walls with $k_s = 5$ µm
- Shrouded wheel, rough walls with $k_s = 5$ µm

This study is undertaken by using the CFD tool based on ANSYS-CFX. Each case corresponds to a different wheel mesh: open wheels require the introduction of the tip clearance and the corresponding geometrical discretization, while wall functions accounting for roughness ask for a first-cell distance from the wall compatible with the roughness level. The cell distribution in the free stream is retained among different cases.

Figure 11 reports the total-to-total efficiency for the four examined cases. Both roughness and tip clearance appreciably affect the efficiency. The shrouded design, which was eventually selected for the CO2OLHEAT project after a considerable effort to ensure structural reliability, has an efficiency that is 3.6% higher than the unshrouded counterpart. Regarding the roughness, the indicated value is just a representative value for the roughness level and not indicative of the manufacturer's capabilities. Nonetheless, the viscous sublayer is estimated to be of the order of $10^{-3} - 10^{-2}\ \mu m$, thus one might expect that, in this kind of machine, the surface roughness will alter the development of the boundary layer and the associated entropy generation. For this specific study, it was found that a sand-grain roughness of 5 μm produces a 2.3% of efficiency drop. This result confirms that roughness effects can be significant and suggests care in the selection of the manufacturing process.

The analysis is extended by decomposing each component contribution to overall loss. The following loss coefficients are introduced for the nozzle and wheel, respectively:

$$\Delta\eta_N = \frac{h(P_{t2}, s_2) - h(P_{t2}, s_0)}{h_{t0} - h_{t6,is}} \tag{21}$$

$$\Delta\eta_W = \frac{h(P_{t6}, s_6) - h(P_{t6}, s_2)}{h_{t0} - h_{t6,is}} \tag{22}$$

Figure 12 reports the loss coefficients for the four examined cases. Leaving aside the cases with open wheels, for which the tip clearance loss dominates in the overall loss generation, the largest share of entropy is however generated in the wheel, which is responsible for an efficiency reduction of 0.9-1.5 percentage points more than the nozzle depending on smooth/rough wall modelling, respectively. Besides friction loss, which prevails in the wheel because of the larger wetted surface, the analysis of the flow field reveals a flow separation along the wheel suction side at 75% of the span. Further, the negative incidence generates a small flow separation after the leading edge on the pressure side. Nonetheless, the generated entropy is relatively small compared to the suction-side separation, and the flow reattaches almost immediately.

Finally, comparing the flow fields between roughness- and smooth-wall simulations, secondary flow structures do not change, and the increase of entropy by adding roughness is

DOI: 10.17185/duepublico/77327

provided by an increase in the profile loss due to boundary-layer thickening. Consistently, the roughness raises wheel losses more than nozzle losses because of the larger wetted surface of the former than the latter.

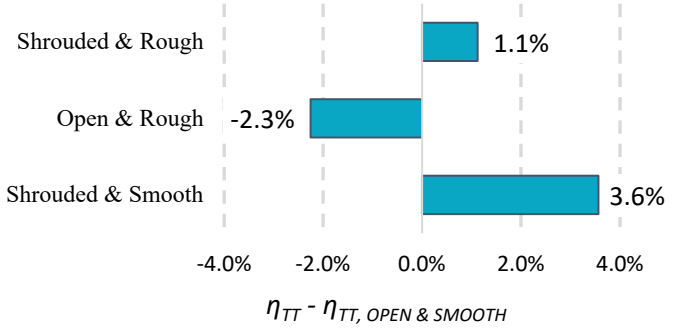

Figure 11: Variations in total-to-total efficiency by introducing the roughness and tip clearance.
© 2022 Baker Hughes Company - All rights reserved

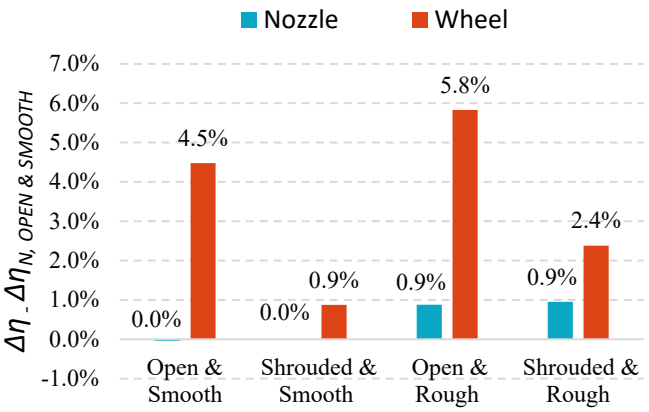

Figure 12: Loss decomposition in nozzle and wheel for the examined cases.
© 2022 Baker Hughes Company - All rights reserved

CONCLUSION

This paper has examined the workflow that has led to the definition of the turbine in the turboexpander unit of the CO2OLHEAT project. The high power density of the sCO_2 power system coupled with high operating pressures dictates low volumetric flows, therefore a radial-inflow turbine was selected as the most promising architecture. The overall expansion ratio was split into two consecutive radial-inflow stages, which were arranged in a back-to-back configuration to balance axial thrusts. The aerodynamic stage design stemmed from the selection of a few characteristic design parameters, namely specific speed and spouting-to-peripheral velocity ratio. After this first step, a preliminary turbine design was accomplished by using a validated mean-line tool.

The turbine performance was assessed by means of two independent CFD studies, which agree remarkably well with minor quantitative differences (< 0.2%). A comparison between the mean line and the CFD estimates confirmed *a posteriori* the good predicting capability of the former, which had laid the foundation for the whole turbine design.

Finally, the effects of clearance and roughness were investigated. These non-scalable geometrical parameters were deemed to be relevant for turbine performance owing to the small scale of the machine. It was found that a clearance-to-diameter ratio of 0.03 yields an efficiency drop of 3.6%. In the same vein, a sand-grain roughness of 5 μm reduces the efficiency by 2.3%. The impact of the clearance has convinced the manufacturer to select a shrouded wheel after a considerable effort to ensure structural reliability. Advanced manufacturing processes will be possibly considered to minimize surface roughness. As a future follow-up activity, unsteady simulations at design and off-design conditions will be performed to assess the impact of non-stationary interactions on the performance, and the aeromechanical forcing on the system.

NOMENCLATURE

b	Spanwise height
BF	Blockage factor
c	Absolute velocity
ch	Chord
D	Diameter
h	Specific enthalpy
I	Rothalpy
k_s	Sand-grain roughness
L	Length
m	Mass flow
M	Mach number
N	Rotational speed
N_s	Specific speed
p	Pressure
Q	Volume flow rate
r	Radius
Re	Reynolds number
s	Specific entropy
t	Thickness
T	Temperature
u	Peripheral speed
w	Relative velocity
Y	Mach expression factor at section i, $Y_i = \left[1 + \frac{\gamma_i - 1}{2} M_i^2\right]^{\frac{\gamma_i}{1-\gamma_i}}$
y^+	Dimensionless distance from solid wall
Z	Blade count

Greek:

α	Absolute flow angle

DOI: 10.17185/duepublico/77327

β	Relative flow angle
γ	Specific heats ratio
Δ	Variation
ε	Clearance
η	Efficiency
φ	Flow coefficient
μ	Dynamic viscosity
ρ	Density

Subscript

a	Axial direction
cl	Clearance
df	Disk Friction
H	Hydraulic
inc	Incidence
is	Isentropic state
N	Nozzle
pe	Post-expansion
pl	Passage loss
r	Radial direction
rel	Referred to the relative frame
rms	Root Mean Square Value
s	Static quantity
t	Total quantity
te	Trailing edge
θ	Tangential direction
vs	Vaneless Space
W	Wheel

ACKNOWLEDGEMENTS

The CO2OLHEAT project has received funding from the European Union's Horizon 2020 research and innovation programme under grant agreement N° 101022831.

REFERENCES

[1] O. Reimann, "CEWEP Energy Report III (Status 2007-2010)," Confederation of European Water-to-Energy Plants, www.cewep.eu, 2012.

[2] M. Marchionni, G. Bianchi and S. Tassou, "Review of supercritical carbon dioxide (sCO2) technologies for high-grade waste heat to power conversion," *SN Applied Sciences,* vol. 2, no. 4, pp. 1-13, 2020.

[3] A. Romei, P. Gaetani, A. Giostri and G. Persico, "The role of turbomachinery performance in the optimization of supercritical carbon dioxide power systems," *Journal of Turbomachinery,* vol. 142, no. 7, p. 071001, 2020.

[4] D. Alfani, M. Binotti, E. Macchi, P. Silva and M. Astolfi, "sCO2 Power Plants for Waste Heat Recovery: Design Optimization and Part-Load Operation Strategies," *Applied Thermal Engineering,* vol. 195, 2021.

[5] R. Pecnik, E. Rinaldi and P. Colonna, "Computational fluid dynamics of a radial compressor operating with supercritical CO2," *Journal of Engineering for Gas Turbines and Power,* vol. 134, no. 12, 2012.

[6] S. Saxena, R. Mallina, F. Moraga and D. Hofer, "Numerical Approach for Real Gas Simulations: Part II – Flow Simulation for Supercritical CO2 Cen-trifugal Compressor," in *ASME Turbo Expo 2017*, 2017.

[7] A. Hosangadi, Z. Liu, T. Weathers, V. Ahuja and J. Busby, "Modeling multiphase effects in CO2 compressors at subcritical inlet conditions," *Journal of Engineering for Gas Turbines and Power,* vol. 141, no. 8, 2019.

[8] G. Persico, P. Gaetani, A. Romei, L. Toni, E. Bellobuono and R. Valente, "Implications of phase change on the aerodynamics of centrifugal compressors for supercritical carbon dioxide applications," *Journal of Engineering for Gas Turbines and Power,* vol. 143, no. 4, 2021.

[9] J. Mortzheim, D. Hofer, S. Piebe, A. McClung, J. J. Moore and S. Cich, "Challenges With Measuring Supercritical CO2 Compressor Perform-ance When Approaching the Liquid-Vapor Dome," in *ASME Turbo Expo 2021*, 2021.

[10] L. Toni, E. Bellobuono, R. Valente, A. Romei, P. Gaetani and G. Persico, "Computational and Experimental Assessment of a MW-Scale Supercritical CO2 Compressor Operating in Multiple Near-Critical Conditions," *Journal of Engineering for Gas Turbines and Power,* vol. 144, no. 10, 2022.

[11] S. D. Cich, J. Jeffrey Moore, M. Marshall, K. Hoopes, J. Mortzheim and D. Hofer, "Radial Inlet and Exit Design for a 10 MWe sCO2 Axial Turbine," in *ASME Turbo Expo 2019*, 2019.

[12] T. El Samad, J. Amaral Teixeira and J. Oakey, "Investigation of a Radial Turbine Design for a Utility-Scale Supercritical CO2 Power Cycle," *Applied Sciences,* vol. 10, no. 12, 2020.

[13] D. Alfani, M. Asolfi, M. Binotti, P. Silva and G. Persico, "Part load analysis of a constant inventory supercritical co2 power plant for waste heat recovery in cement industry," in *The 5th European sCO2 Conference for Energy Systems*, 2023.

[14] F. Lottini, M. Marconcini, A. Arnone, D. Biliotti and L. Toni, "Numerical investigation on radial turbines aerodynamics aimed at the definistion of design rules for industrial applications," *Proceedings of ASME Turbo Expo 2022,* 2022.

[15] E. Lemmon, I. Bell, M. Huber and M. McLinden, *NIST Standard Reference Database 23: Reference Fluid Thermodynamic and Transport Properties-REFPROP, Version 10.0, National Institute of Standards and Technology,* 2018.

[16] H. Rohlik, Kofskey and Milton, "Recent radial turbine research at the NASA Lewis Research Center," *American Society of Mechanical Engineers,* vol. 79818, 1972.

[17] C. Rodgers, "Mainline performance prediction for radial inflow turbines," *Von Karman Inst. for Fluid Dynamics,* 1987.

DOI: 10.17185/duepublico/77327

[18] A. Glassman, "Enhanced analysis and users manual for radial-inflow turbine conceptual design code RTD," NASA, 1995.

[19] R. H. Aungier, Turbine aerodynamics, New York: American Society of Mechanical Engineers Press, 2006.

[20] L. J. Kastner and F. S. Bhinder, "A method for predicting the performance of a centripetal gas turbine fitted with a nozzle-less volute casing," in *American Society of Mechanical Engineers*, 1975.

[21] N. C. Baines, "A meanline prediction method for radial turbine efficiency," 1998.

[22] J. W. Daily and R. E. Nece, "Chamber Dimension Effects on Induced Flow and Frictional Resistance of Enclosed Rotating Disks," *Journal of Fluids Engineering,* vol. 82, no. 1, p. 217–230, 1 March 1960.

[23] A. Meroni, M. Robertson, R. Martinez-Botas and F. Haglind, "A methodology for the preliminary design and performance prediction of high-pressure ratio radial-inflow turbines," *Energy,* vol. 164, pp. 1062--1078, 2018.

[24] D. Fiaschi, G. Manfrida and F. Maraschiello, "Design and performance prediction of radial ORC turboexpanders," *Applied Energy,* vol. 138, pp. 517--532, 2015.

[25] A. Arnone, "Viscous analysis of three-dimensional rotor flow using a multigrid method," 1994.

[26] P. Boncinelli, F. Rubechini, A. Arnone, M. Cecconi and C. Cortese, "Real Gas Effects in Turbomachinery Flows: a CFD Model for Fast Computations," *ASME J. Turbomach.,* vol. 162, no. 2, pp. 268-276, 2004.

[27] M. Marconcini, F. Rubechini, A. Arnone, A. Scotti Del Greco and R. Biagi, "Aerodynamic investigation of a high pressure ratio turbo-expander for organic Rankine cycle applications," *Turbo Expo: Power for Land, Sea, and Air,* vol. 44748, pp. 847--856, 2012.

[28] F. Rubechini, M. Marconcini, A. Arnone, A. Scotti Del Greco and R. Biagi, "Special challenges in the computational fluid dynamics modeling of transonic turbo-expanders," *Journal of engineering for gas turbines and power,* vol. 135, 2013.

[29] R. Pacciani, M. Marconcini and A. Arnone, "Comparison of the AUSM+-up and other advection schemes for turbomachinery applications," *Shock Waves,* vol. 29, pp. 705--716, 2019.

[30] D. C. Wilcox, Turbulence modeling for CFD, vol. 2, DCW industries La Canada, CA, 1998.

DOI: 10.17185/duepublico/77327

DuEPublico

Duisburg-Essen Publications online

UNIVERSITÄT DUISBURG ESSEN

Offen im Denken

ub | universitäts bibliothek

Published in: 5th European sCO2 Conference for Energy Systems, 2023

This text is made available via DuEPublico, the institutional repository of the University of Duisburg-Essen. This version may eventually differ from another version distributed by a commercial publisher.

DOI: 10.17185/duepublico/77327
URN: urn:nbn:de:hbz:465-20230427-145822-3

This work may be used under a Creative Commons Attribution 4.0 License (CC BY 4.0).